Physica E 119 (2020) 113999

Contents lists available at ScienceDirect

Physica E: Low-dimensional Systems and Nanostructures

journal homepage: www.elsevier.com/locate/physe

Enhancement of the Fano-resonance response in bilayer graphene single and double barriers induced by bandgap opening

J.A. Briones-Torres [a], R. Pérez-Álvarez [a], R. Pernas-Salomón [b], I. Rodríguez-Vargas [c,*]

[a] Centro de Investigación en Ciencias, Universidad Autónoma del Estado de Morelos, Av. Universidad 1001 Col. Chamilpa, 62209 Cuernavaca, Morelos, Mexico
[b] Faculty of Mechanical Engineering, Technion–Israel Institute of Technology, Haifa 32000, Israel
[c] Unidad Académica de Ciencia y Tecnología de la Luz y la Materia, Universidad Autónoma de Zacatecas, Carretera Zacatecas-Guadalajara Km. 6, Ejido La Escondida, 98160 Zacatecas, Zac., Mexico

ARTICLE INFO

Keywords:
Fano resonances
Bilayer graphene
Bandgap opening
Single barriers
Double barriers

ABSTRACT

Fano resonances in bilayer graphene arise due to the coupling between extended and discrete electrons states, and represent an exotic phenomenon in graphene akin to Klein and anti-Klein tunneling, atomic collapse and negative refraction to mention a few. The hallmark of these resonances is identifiable in the conductance curves of bilayer graphene barrier structures. Furthermore, the Fano line-shape can be presented in the conductance by reducing the angular range in the computation of the transport properties. In this work, we explore the possible consequences that bandgap opening in the band structure of bilayer graphene can have over Fano resonances. We have used a four-band Hamiltonian to taking into account the mentioned band structure modifications. The hybrid matrix method and the Landauer–Büttiker formalism have been implemented to obtain the transmittance and the conductance, respectively. We find that the signatures of the Fano resonances on the conductance are enhanced by the opening of the bandgap. In fact, the Fano profile is manifested in the conductance without the need of reducing the angular range. This enhancement results from the improvement of the chirality matching between extended and discrete states induced by the bandgap opening. The main characteristics of the impact of the bandgap opening on the transmission and transport properties of single and double barriers are presented. So, the bandgap opening far from hamper the Fano resonance response promotes it and can be used as modulation parameter to prove the exotic phenomenon of Fano resonances in bilayer graphene barrier structures.

1. Introduction

Bilayer graphene has become a material that promises great things in nanotechnology [1–3]. Its outstanding properties such as excellent electrical conductivity [4], high thermal conductivity [5], the possibility of modulating its electrical properties through doping [6,7], among many other put it to compete against its monolayer counterpart, monolayer graphene or simply graphene. In particular, bilayer graphene has a strong advantage due to the possibility of opening a bandgap and/or doping it through the application of electrostatic fields [8,9]. Bilayer graphene can be obtained by micromechanical exfoliation [10], its more stable arrangement is known as Bernal, unlike monolayer graphene it has a structure of four hyperbolic bands, two of them touching in the **K** point at zero energy and the other two separated by an energy of $\gamma_1 = 390$ meV [3].

Regarding exotic effects, monolayer graphene is the 2D material per excellence. For instance, Klein tunneling [11,12], atomic collapse [13,14], Hofstadter's butterfly [15,16] and negative refraction [17,18] have been confirmed experimentally in this material. Practically all these exotic phenomena owe its existence to the special band structure as well as the quantum relativistic chiral nature of the charge carriers [10,11]. Under this context, bilayer graphene is not the exception and exotic effects such as anti-Klein tunneling [11,19], cloaked states [19,20], unconventional superconductivity [21,22] and Fano resonances [23–26] have been reported. In this case the gapless parabolic band structure and the massive chiral character of the charge carriers give rise to these peculiar phenomena. In particular, anti-Klein tunneling is the perfect reflection of the charge carriers through electrostatic barriers at normal incidence [11,19]. This effect is the result of the pseudo-spin conservation and the Berry phase 2π of bilayer graphene [6]. Cloaked states are nearly invisible confined states inside electrostatic barriers [19,20]. In this case the chiral mismatch between charge carriers inside and outside the barriers is what makes confined states invisible to charge carriers propagating through the

* Corresponding author.
E-mail address: isaac@uaz.edu.mx (I. Rodríguez-Vargas).

https://doi.org/10.1016/j.physe.2020.113999
Received 23 October 2019; Received in revised form 9 January 2020; Accepted 30 January 2020
Available online 3 February 2020

barriers. This phenomenon takes place at normal incidence and is intimately related to anti-Klein tunneling [19]. Another effect that can be induced in bilayer graphene is superconductivity [21,22]. By twisting the graphene layers at a magic angle of 1.1° a strong correlated phase typical of unconventional superconductors can arise [21]. This rather exotic phase is owing to the flattening of the band structure through the twist angle as well as to the doping by simply gating bilayer graphene. In the case of Fano resonances, the coupling between propagating and confined states in electrostatic barriers at oblique incidence gives rise to the typical asymmetrical line-shape of these special resonances in the electron transmittance [23–25]. The Fano profile is quite sensitive to the angle of incidence and Fano resonances can also be shifted readily by changing the structural parameters of the barriers. Furthermore, Fano resonances can leave a hallmark in the transport properties, specifically the conductance [26]. Even more, by reducing the angular range in the computation of the transport properties the conductance curves can manifest a Fano profile. In bilayer graphene double barriers and superlattices the coupling between Fano resonances and resonant (miniband) states gives rise to the so called hybrid resonances [26]. The contribution of these resonances can be tracked and identified in the conductance curves. Fano resonances can be considered as exotic as anti-Klein tunneling, cloaked states and unconventional superconductivity because with simple electrostatic barriers we can have them. This is in stark contrast with the typical systems in which Fano resonances arise [27]. For instance, systems in which the superposition of configurations with discrete states and propagating states give rise to asymmetrical line-shapes in optical properties. Typically, a light source, a magnetic field or some other physical effect plays the role of mixing between discrete and continuum states. Other typical systems are intricate quantum dots that assure the coupling between system configurations with confined and continuum states and consequently the asymmetrical line-shape of Fano resonances in the quantum conductance. For more details about these typical systems the reader is remitted to the excellent review of Miroshnichenko and colleagues [27]. Even more, these Fano resonances that are the result of the chiral matching between electron states inside and outside the barriers are quite distinct to other Fano resonances that can arise in bilayer graphene due to the interplay between light, electrons and phonons [28,29]. In principle, these exotic electron Fano resonances can be tested experimentally through transport experiments as the anti-Klein tunneling [20], cloaked states [20] and unconventional superconductivity [22]. An applied electric field or simply gating has been fundamental in corroborating these phenomena. With gating we can create electrostatic barriers and/or doped bilayer graphene. Gating is also technologically appealing because a bandgap in the band structure of bilayer graphene can be induced. However, bandgap opening can disrupt the delicate conditions that give rise to the mentioned exotic effects. For instance, Lu et al. [30] report that anti-Klein tunneling can be destroyed by the resonant states induced by a multi-barrier structure in bilayer graphene. Even, the destruction can take place in the presence of a bandgap. In the case of Fano resonances, as far as we know, there is no a detail study that tells us to what extent bandgap opening can disrupt, modify or even destroy them. This could be quite relevant because if a tiny bandgap destroys the characteristic asymmetrical line-shape of Fano resonances can be really challenging to corroborate this phenomenon experimentally.

The aim of this work is to see if Fano resonances are still present when bandgap opening is considered in the band structure of bilayer graphene barrier structures. In order to do that a four-band hamiltonian that accounts for the mentioned band structure modifications has been considered. The transmittance and conductance of bilayer graphene barriers structures are obtained within the lines of the hybrid matrix method and the Landauer–Büttiker formalism, respectively. We find that the bandgap opening promotes the Fano resonance response on the transport properties. In particular, the Fano line-shape is obtained in the conductance without the need of reducing the angular range. The bandgap opening changes the chiral characteristics of the charge carriers in the barrier regions. These changes improve the chiral matching between the Dirac electrons inside and outside the barriers, resulting in an overall enhancement of the Fano resonance response. We carry out a detail analysis of the impact of the bandgap opening on the transmission and transport properties of single and double barrier structures. In concrete, we focus our attention in the modifications induced by the bandgap opening on Fano and hybrid resonances, which are natural in single and double barriers.

2. Methodology

The method we will use is very similar to the Sturm–Liouville formalism and totally compatible with the hybrid matrix method [31–33]. The details are given below. The Hamiltonian that describes charge carriers in bilayer graphene to energies of the order of $\gamma_0 = 3.09$ eV is given as [30,34]

$$\mathbf{H} = \begin{pmatrix} V_1 & \pi & t_\perp & 0 \\ \pi^* & V_1 & 0 & 0 \\ t_\perp & 0 & V_2 & \pi^* \\ 0 & 0 & \pi & V_2 \end{pmatrix}, \tag{1}$$

where $\pi = v_F(p_x + ip_y)$, $\pi^* = v_F(p_x - ip_y)$, also, $p_{x,y} = -i\hbar\partial_{x,y}$ is the moment operator, v_F is the Fermi Velocity, $t_\perp = 390$ meV describes the interaction between layers that meet the potentials V_1 and V_2. Here, it is important to mention that this hamiltonian takes into account bandgap opening (when $V_1 \neq V_2$) and non-parabolicity in the band structure of bilayer graphene.

Using the eigenvalue equation and some basic rules of matrices,[1] we can arrive at

$$\frac{d\mathbf{F}(x)}{dx} + \begin{pmatrix} q_y & i\frac{V_1-E}{\hbar v_F} & 0 & 0 \\ i\frac{V_1-E}{\hbar v_F} & -q_y & i\frac{t_\perp}{\hbar v_F} & 0 \\ 0 & 0 & -q_y & i\frac{V_2-E}{\hbar v_F} \\ i\frac{t_\perp}{\hbar v_F} & 0 & i\frac{V_2-E}{\hbar v_F} & q_y \end{pmatrix} \cdot \mathbf{F}(x) = \mathbf{0}_{4\times1}. \tag{2}$$

If we propose a solution of the form $\mathbf{F} = \mathbf{F}_0 e^{iqx}$, and substitute it in the previous equation, we obtain

$$\begin{pmatrix} q_y + iq & i\frac{V_1-E}{\hbar v_F} & 0 & 0 \\ i\frac{V_1-E}{\hbar v_F} & -q_y & i\frac{t_\perp}{\hbar v_F} & 0 \\ 0 & 0 & -q_y + iq & i\frac{V_2-E}{\hbar v_F} \\ i\frac{t_\perp}{\hbar v_F} & 0 & i\frac{V_2-E}{\hbar v_F} & q_y + iq \end{pmatrix} \cdot \mathbf{F}_0 = \Theta(q) \cdot \mathbf{F}_0 = \mathbf{0}_{4\times1}. \tag{3}$$

To obtain the q-values that vanish the determinant of the secular matrix $\Theta(q)$ we solve the fourth-order equation in q. Then we obtain analytic expressions for the four eigenvalues

$$q = \pm\sqrt{-q_y^2 - \frac{1}{2(\hbar v_F)^2}[(E-V_1)^2+(E-V_2)^2] \pm \frac{1}{2(\hbar v_F)^2}\sqrt{[(E-V_1)^2-(E-V_2)^2]^2+4t_\perp(E-V_1)(E-V_2)}}. \tag{4}$$

These eigenvalues appear in pairs of the type $(q, -q)$. In particular, the pairs $(q_1, -q_1)$ and $(q_2, -q_2)$ correspond to the plus (+) and minus (−) sign inside the square root, respectively. Here, it is important to mention that q_2 is pure imaginary, giving rise to evanescent modes. Furthermore, the wavefunction amplitudes are given by

$$\mathbf{F}_{0j}^{\pm} = (a_j, b_j^{\pm}, c_j, d_j^{\pm})^T, \quad j = 1, 2. \tag{5}$$

where the components are

$$a_j = i\frac{E - V_1}{\hbar v_F}; \tag{6}$$

[1] Including the fact that there is homogeneity in the vertical axis, that is, $q_y = k_y$.

$$b_j^{\pm} = q_y \pm iq_j; \tag{7}$$

$$c_j = \frac{i}{t_\perp \hbar v_F}[(E-V_1)^2 - (q_y^2+q_j^2)(\hbar v_F)^2]; \tag{8}$$

$$d_j^{\pm} = \frac{t_\perp^2(E-V_1) - (E-V_2)[(E-V_1)^2 - (q_y^2+q_j^2)(\hbar v_F)^2]}{(q_y \pm iq_j)t_\perp(\hbar v_F)^2}. \tag{9}$$

Then, the linear independent solutions can be expressed as

$$\mathbf{F}_{01}^{+}e^{iq_1x}, \mathbf{F}_{01}^{-}e^{-iq_1x}, \mathbf{F}_{02}^{+}e^{iq_2x}, \mathbf{F}_{02}^{-}e^{-iq_2x}. \tag{10}$$

Any general solution can be expressed as a linear combination of these linearly independent solutions. In matrix form this combination can be written as

$$\mathbf{F}(x) = \begin{pmatrix} a_1e^{iq_1x} & a_2e^{iq_2x} & a_1e^{-iq_1x} & a_2e^{-iq_2x} \\ b_1^{+}e^{iq_1x} & b_2^{+}e^{iq_2x} & b_1^{-}e^{-iq_1x} & b_2^{-}e^{-iq_2x} \\ c_1e^{iq_1x} & c_2e^{iq_2x} & c_1e^{-iq_1x} & c_2e^{-iq_2x} \\ d_1^{+}e^{iq_1x} & d_2^{+}e^{iq_2x} & d_1^{-}e^{-iq_1x} & d_2^{-}e^{-iq_2x} \end{pmatrix} \cdot \begin{pmatrix} \alpha_1^{+} \\ \alpha_2^{+} \\ \alpha_1^{-} \\ \alpha_2^{-} \end{pmatrix}. \tag{11}$$

We want to use a method that is numerically stable, as the Hamiltonian does not involve second derivates, we cannot directly apply the Sturm–Liouville formalism and the hybrid matrix method in its usual form [31–33]. Instead, we will re-write our fundamental equations in order to define an equivalent numerically stable hybrid matrix. Details about the stability and reliability of the present hybrid matrix can be found in the Supplementary Information. To find the corresponding matrix for some homogeneous domain (in our case barriers or wells) we express Eq. (11) in matrix blocks,

$$\mathbf{F}(x) = \begin{pmatrix} \mathbf{F}_u(x) \\ \mathbf{F}_d(x) \end{pmatrix} = \begin{pmatrix} \mathbf{U}^{+}(x) & \mathbf{U}^{-}(x) \\ \mathbf{D}^{+}(x) & \mathbf{D}^{-}(x) \end{pmatrix} \cdot \begin{pmatrix} \alpha^{+} \\ \alpha^{-} \end{pmatrix}. \tag{12}$$

As $\mathbf{F}(x)$ is a four-component vector, then $\mathbf{F}_u(x)$ is a column vector formed by the first two components and $\mathbf{F}_d(x)$ is a column vector formed by the other two components. $\mathbf{U}^{\pm}(x)$ and $\mathbf{D}^{\pm}(x)$ are the 2×2 respective blocks of the 4×4 matrix in Eq. (11). Using the definition of the hybrid matrix that relates the vectors $\mathbf{F}_u(x)$ and $\mathbf{F}_d(x)$ at the ends x_L and x_R of the heterostructure, we can write the following equation,

$$\begin{pmatrix} \mathbf{F}_u(x_L) \\ \mathbf{F}_d(x_R) \end{pmatrix} = \mathbf{H}(x_R, x_L) \cdot \begin{pmatrix} \mathbf{F}_d(x_L) \\ \mathbf{F}_u(x_R) \end{pmatrix}. \tag{13}$$

Making use of Eqs. (12) and (13) we obtain that

$$\mathbf{H}(x_R, x_L) = \begin{pmatrix} \mathbf{U}^{+}(x_L) & \mathbf{U}^{-}(x_L) \\ \mathbf{D}^{+}(x_R) & \mathbf{D}^{-}(x_R) \end{pmatrix} \cdot \begin{pmatrix} \mathbf{D}^{+}(x_L) & \mathbf{D}^{-}(x_L) \\ \mathbf{U}^{+}(x_R) & \mathbf{U}^{-}(x_R) \end{pmatrix}^{-1}, \tag{14}$$

or, explicitly

$$\mathbf{H}(x_R, x_L) = \begin{pmatrix} a_1e^{iq_1x_L} & a_2e^{iq_2x_L} & a_1e^{-iq_1x_L} & a_2e^{-iq_2x_L} \\ b_1^{+}e^{iq_1x_L} & b_2^{+}e^{iq_2x_L} & b_1^{-}e^{-iq_1x_L} & b_2^{-}e^{-iq_2x_L} \\ c_1e^{iq_1(x_R)} & c_2e^{iq_2(x_R)} & c_1e^{-iq_1(x_R)} & c_2e^{-iq_2(x_R)} \\ d_1^{+}e^{iq_1(x_R)} & d_2^{+}e^{iq_2(x_R)} & d_1^{-}e^{-iq_1(x_R)} & d_2^{-}e^{-iq_2(x_R)} \end{pmatrix} \cdot \begin{pmatrix} c_1e^{iq_1x_L} & c_2e^{iq_2x_L} & c_1e^{-iq_1x_L} & c_2e^{-iq_2x_L} \\ d_1^{+}e^{iq_1x_L} & d_2^{+}e^{iq_2x_L} & d_1^{-}e^{-iq_1x_L} & d_2^{-}e^{-iq_2x_L} \\ a_1e^{iq_1(x_R)} & a_2e^{iq_2(x_R)} & a_1e^{-iq_1(x_R)} & a_2e^{-iq_2(x_R)} \\ b_1^{+}e^{iq_1(x_R)} & b_2^{+}e^{iq_2(x_R)} & b_1^{-}e^{-iq_1(x_R)} & b_2^{-}e^{-iq_2(x_R)} \end{pmatrix}^{-1}. \tag{15}$$

This is the hybrid matrix for a homogeneous domain. To obtain the hybrid matrix of a heterostructure it is necessary to apply the composition rule of this matrix [31]. And with this we can easily calculate the transmission and transport properties. First, to calculate the transmittance, suppose that the left and right extremes of the structure have coordinates x_L and x_R. Then we will assume that a wave $\mathbf{F}_{01}^{+}e^{iq_1x}$ hits the left end and results in reflections $\mathbf{F}_{01}^{-}e^{-iq_1x}$ and $\mathbf{F}_{02}^{-}e^{-iq_2x}$ in that domain, while at the right end we have only transmitted waves $\mathbf{F}_{01}^{+}e^{iq_1x}$ and $\mathbf{F}_{02}^{+}e^{iq_2x}$.

For the left and right semi-infinite regions we can write

$$\begin{pmatrix} \mathbf{F}_u(x_L) \\ \mathbf{F}_d(x_R) \end{pmatrix} = \begin{pmatrix} a_{1L}\alpha_{1L}^{+} + a_{1L}\alpha_{1L}^{-} + a_{2L}\alpha_{2L}^{-} \\ b_{1L}^{+}\alpha_{1L}^{+} + b_{1L}^{-}\alpha_{1L}^{-} + b_{2L}^{-}\alpha_{2L}^{-} \\ c_{1R}\alpha_{1R}^{+} + c_{2R}\alpha_{2R}^{+} \\ d_{1R}^{+}\alpha_{1R}^{+} + d_{2R}^{+}\alpha_{2R}^{+} \end{pmatrix}, \tag{16}$$

and

$$\begin{pmatrix} \mathbf{F}_d(x_L) \\ \mathbf{F}_u(x_R) \end{pmatrix} = \begin{pmatrix} c_{1L}\alpha_{1L}^{+} + c_{1L}\alpha_{1L}^{-} + c_{2L}\alpha_{2L}^{-} \\ d_{1L}^{+}\alpha_{1L}^{+} + d_{1L}^{-}\alpha_{1L}^{-} + d_{2L}^{-}\alpha_{2L}^{-} \\ a_{1R}\alpha_{1R}^{+} + a_{2R}\alpha_{2R}^{+} \\ b_{1R}^{+}\alpha_{1R}^{+} + b_{2R}^{+}\alpha_{2R}^{+} \end{pmatrix}. \tag{17}$$

For these equations we are considering reduced bases at x_L and x_R, that is, we are changing x to $x-x_L$ and $x-x_R$, respectively. The subscripts L and R indicate the external domain where the coefficients and parameters are calculated. We are also discarding the coefficients α_{1R}^{-} and α_{2R}^{-} in the right domain because there is no reflected wave and as q_2 is pure imaginary a diverging wave is not physically acceptable. For the left domain we set $\alpha_{2L}^{+}=0$ because it represents a diverging wave. We can also define the reflection and transmission amplitudes as $r_1=\alpha_{1L}^{-}/\alpha_{1L}^{+}$, $r_2=\alpha_{2L}^{-}/\alpha_{1L}^{+}$, $t_1=\alpha_{1R}^{+}/\alpha_{1L}^{+}$ and $t_2=\alpha_{2R}^{+}/\alpha_{1L}^{+}$. With this, Eq. (13) takes the form

$$\mathbf{M}_1 + \mathbf{M}_2 \cdot \begin{pmatrix} r_1 \\ r_2 \\ t_1 \\ t_2 \end{pmatrix} = \mathbf{H}(x_R, x_L) \cdot \mathbf{M}_3 + \mathbf{H}(x_R, x_L) \cdot \mathbf{M}_4 \cdot \begin{pmatrix} r_1 \\ r_2 \\ t_1 \\ t_2 \end{pmatrix}, \tag{18}$$

where the matrices $\mathbf{M}_1, \mathbf{M}_2, \mathbf{M}_3$ and $\mathbf{M}_4$ are given as

$$\mathbf{M}_1 = \begin{pmatrix} a_{1L} \\ b_{1L}^{+} \\ 0 \\ 0 \end{pmatrix}, \quad \mathbf{M}_2 = \begin{pmatrix} a_{1L} & a_{2L} & 0 & 0 \\ b_{1L}^{-} & b_{2L}^{-} & 0 & 0 \\ 0 & 0 & c_{1R} & c_{2R} \\ 0 & 0 & d_{1R}^{+} & c_{2R}^{+} \end{pmatrix}, \tag{19}$$

$$\mathbf{M}_3 = \begin{pmatrix} c_{1L} \\ d_{1L}^{+} \\ 0 \\ 0 \end{pmatrix}; \quad \mathbf{M}_4 = \begin{pmatrix} c_{1L} & c_{2L} & 0 & 0 \\ d_{1L}^{-} & d_{2L}^{-} & 0 & 0 \\ 0 & 0 & a_{1R} & a_{2R} \\ 0 & 0 & b_{1R}^{+} & b_{2R}^{+} \end{pmatrix}. \tag{20}$$

Finally, we get that

$$\begin{pmatrix} r_1 \\ r_2 \\ t_1 \\ t_2 \end{pmatrix} = \left[\mathbf{M}_2 - \mathbf{H}(x_R, x_L) \cdot \mathbf{M}_4\right]^{-1} \cdot \left[\mathbf{H}(x_R, x_L) \cdot \mathbf{M}_3 - \mathbf{M}_1\right]. \tag{21}$$

The transmission probability is given as [23,25]

$$T = \frac{j_{x,1R}^{+}}{j_{x,1L}^{+}}, \tag{22}$$

where $j_{x,1R}^{+}$ represents the transmitted probability current density and $j_{x,1L}^{+}$ the incident one. As the left and right semi-infinite regions are the same Eq. (22) can be reduced to

$$T = \left|\frac{\alpha_{1R}^{+}}{\alpha_{1L}^{+}}\right|^2, \tag{23}$$

with $\alpha_{1R}^{+}/\alpha_{1L}^{+}$ the amplitude of the outgoing/incoming wave of the right/left semi-infinite region. So, according to the definition of t_1, then $T=|t_1|^2$ [34].

To calculate the transport properties, particularly the linear-regime conductance, we will use the Landauer–Büttiker formalism [35]. Within this formalism the conductance comes as

$$\frac{G}{G_0} = \int_{-\frac{\pi}{2}}^{\frac{\pi}{2}} T(E_F, \theta)\cos\theta d\theta, \tag{24}$$

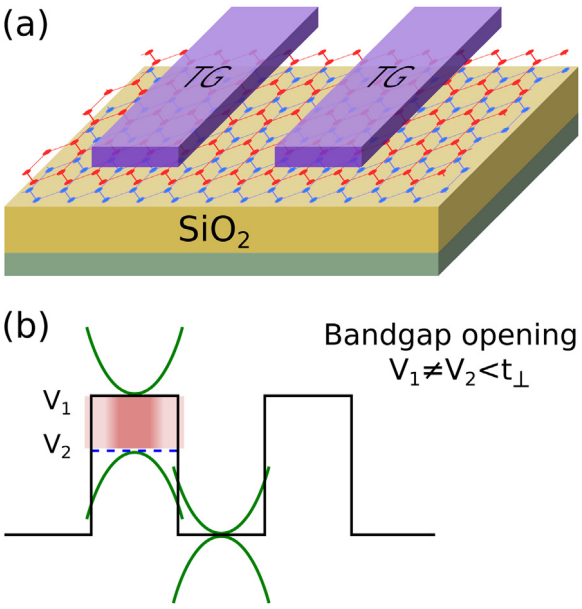

Fig. 1. (a) Schematic representation of the possible device for bilayer graphene barrier structures. The graphene layers are placed between dielectric substrates, like SiO_2 and Al_2O_3, that in conjunction with back and top gates can shift the energy band structure, open a band gap and even dope the material [8,9]. (b) Potential energy diagram for double barriers along the x-coordinate (propagation direction). In this case the potential energy in the top (V_1) and the bottom (V_2) layers is not the same, giving rise to a band gap $E_g = V_1 - V_2$, red-shaded area. It is also considered that V_1 and V_2 are below the interlayer coupling energy $t_\perp$ such that the bands can be assumed as parabolic. (For interpretation of the references to color in this figure legend, the reader is referred to the web version of this article.)

where $G_0 = \frac{2e^2 L_y E_F}{h^2 v_F}$ is the fundamental conductance factor.

3. Results and discussions

In Fig. 1a a schematic representation of the system that we are interested in is shown. It consists in two graphene layers sandwiched between dielectric slabs, such as SiO_2 and Al_2O_3, and top and back gates. With this device configuration it is possible to shift the bilayer graphene band structure, energetically speaking, open a bandgap on it and even dope the material [8,9]. Then, in principle, with an arrangement of top gates we can obtain single and double barrier potentials. In particular, we are interested in single and double barrier potentials in which the graphene layers in the top gated regions have different potential energy, such that a bandgap is present in the structure, $E_g = V_1 - V_2$, red-shaded area in Fig. 1b. It is also assumed that V_1 and V_2 are below the interlayer coupling energy $t_\perp$, hence the energy bands can be considered as parabolic.

The aim of the present work is to analyze to what extent Fano resonances in single barriers and hybrid Fano resonances in double barriers [26] are affected by the presence of a bandgap. So, we will show representative cases in order to unveil the impact of the bandgap on the transmittance and conductance curves for the mentioned barrier structures.

3.1. Single barrier structures

Firstly, we present the results for single barriers. It is well known that Fano resonances arise in single barriers at nearly normal incidence and that they depend strongly on the angle of incidence, the width and the height of the barrier [25,26]. In Fig. 2 we show how a Fano resonance in single barriers is affected by the bandgap opening. As we can notice a well-defined Fano resonance presented at $\theta = 5°$, solid-black curve in (a), is modified once the bandgap is opened. In this case the barrier width is 10 nm, $V_1 = 50$ meV and V_2 is reduced systematically from 50 meV to 0 meV. For a bandgap of $E_g = V_1 - V_2 = 5$ meV the Fano resonance amplitude is reduced and eventually the transmittance profile becomes an anti-resonance for $E_g = 10$ meV. By increasing further the bandgap ($E_g = 15$ meV) an inverted Fano resonance arises, with the maximum at lower energy (left) and the minimum at higher energy (right), see the dotted–dashed-blue curve in (a). For larger bandgaps the inverted Fano resonance is deformed to such point that it is difficult to consider it as the typical asymmetrical line-shape of the Fano profile, see Fig. 2b. We can also see that in effective terms the Fano resonance is shifted to lower energies as the bandgap increases, consequently the discrete state involved. Similar results are obtained if we fixed V_2 at 50 meV and varied V_1 from 50 meV to 100 meV. However, in this case the Fano resonance, in addition to the deformation, is shifted to higher energies (see Fig. 3), which means that the associated discrete state is also shifted to higher energies. In the light of these results it seems that at first instance the bandgap opening is not beneficial to the Fano resonances. However, as we will see in short, the bandgap opening modifies the chiral characteristics of the charge carriers in the barrier region [36], resulting in a more effective chiral matching between states inside and outside the barrier and consequently in an enhancement of the Fano resonance response. In Fig. 4 we show the results of the transmittance at normal incidence ($\theta = 0°$) for various values of the bandgap. As it is well known, in the gapless case there is no coupling between the states inside and outside the barrier and consequently the transmittance does not present any Fano profile, see the solid-black curve in Fig. 4a. As we can notice, once the bandgap is opened a well-defined inverted Fano resonance arises at about 20 meV, dotted-red curve in Fig. 4a. For a bandgap of 20 meV the Fano resonance is shifted to lower energies and the energy distance between the maximum and the minimum is increased, dashed-green curve in Fig. 4a. By further increasing the bandgap, the Fano resonance is progressively moved to lower energies as well as deformed, see Fig. 4b. As in the case of oblique incidence, after some specific bandgap the transmittance curve is deformed to such degree that cannot be considered as the typical asymmetrical line-shape of Fano resonances. Similar results are obtained if we fixed V_2 at 50 meV and varied V_1 from 50 meV to 100 meV in steps of 10 meV. However, in this case the Fano resonance is deformed and shifted to higher energies as the bandgap increases, see Fig. 5.

Now we will analyze to what extent the Fano resonances presented under bandgap opening are affected by the angle of incidence. This is quite relevant because at the end the conductance is the sum over all transmission channels (angles) and if the Fano resonances are manifested in the conductance will depend on its characteristics with the angle of incidence. In Fig. 6 we show the evolution of a Fano resonance as a function of the angle of incidence for bilayer graphene single barriers under a bandgap opening of $E_g = 15$ meV. As we can notice the amplitude of the Fano resonance induced by the bandgap opening is reduced when the angle of incidence increases. In particular, the peak at low energies is systematically diminished and disappears for large angles, see Fig. 6b. Despite the destruction of the Fano profile with the angle of incidence, it is quite relevant that the main contribution to the transport properties will come from the Fano resonances. This opens the possibility of see directly the hallmark of the Fano resonances on the conductance without the need of reducing the angular range. A similar behavior occurs if we consider $V_1 = 65$ meV and $V_2 = 50$ meV, that is, the same bandgap as in Fig. 6, $E_g = 15$ meV. However, in this case the Fano resonance is shifted to higher energies and progressively deformed as the angle of incidence increases (Fig. 7a), losing the asymmetrical line-shape for large angles (Fig. 7b).

Regarding the transport properties turns out that the bandgap opening rather than be prejudicial for the possible detection of the Fano resonances in the conductance curves it is beneficial. For instance, in the gapless case it is necessary to reduce the angular range in order to see the hallmark of the Fano resonances on the conductance,

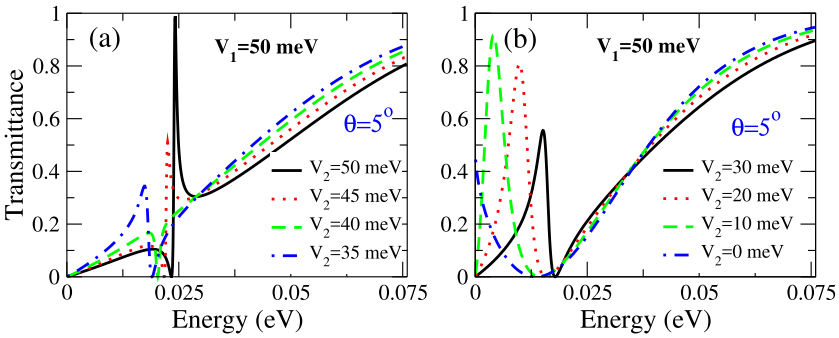

Fig. 2. Bandgap opening effect over a well-defined Fano resonance. An asymmetrical line-shape is presented in gapless bilayer graphene single barriers at oblique incidence, solid-black curve in (a). Once the bandgap is opened the Fano resonance is modified, eventually becoming an anti-resonance as well as an inverted Fano resonance, dotted-red, dashed-green and dotted–dashed-blue lines in (a), respectively. After some critical bandgap the transmittance profile is deformed and cannot be considered as a Fano profile strictly speaking, see curves in (b). Here, the barrier width is 10 nm and the angle of incidence is $\theta = 5°$.

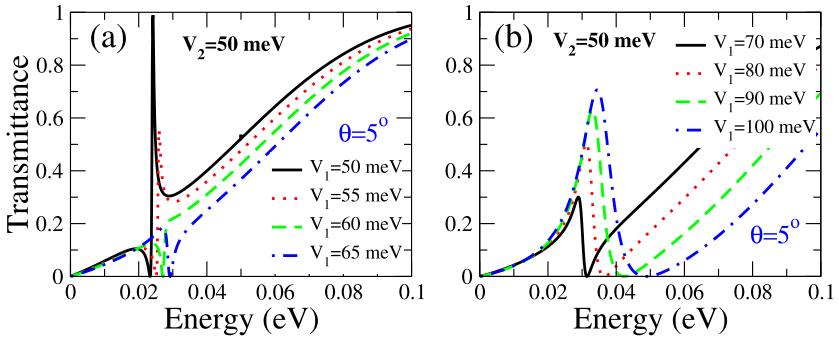

Fig. 3. The same as Fig. 2, but here V_2 is fixed at 50 meV, while V_1 is varied from 50 meV to 100 meV.

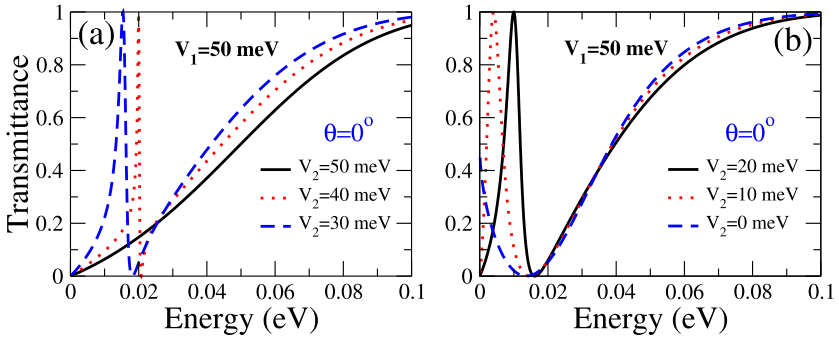

Fig. 4. Influence of the bandgap over the transmission probability at normal incidence, $\theta = 0°$. In (a) the bandgap E_g takes values of 0, 10 and 20 meV, solid-black, dotted-red and dashed-blue lines respectively. In (b) the values for E_g are 30, 40 and 50 meV, solid-black, dotted-red and dashed-blue lines, respectively. As in Fig. 2, the barrier width is 10 nm, V_1 is fixed at 50 meV and V_2 is varied from 50 meV to 0 meV.

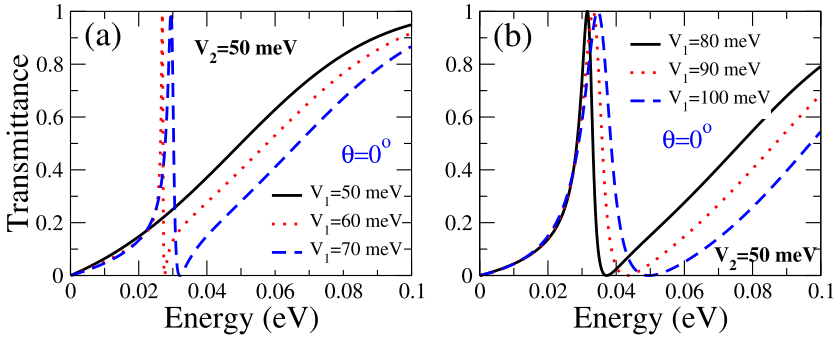

Fig. 5. The same as Fig. 4, but here V_2 is fixed to 50 meV and V_1 is varied from 50 meV to 100 meV in steps of 10 meV.

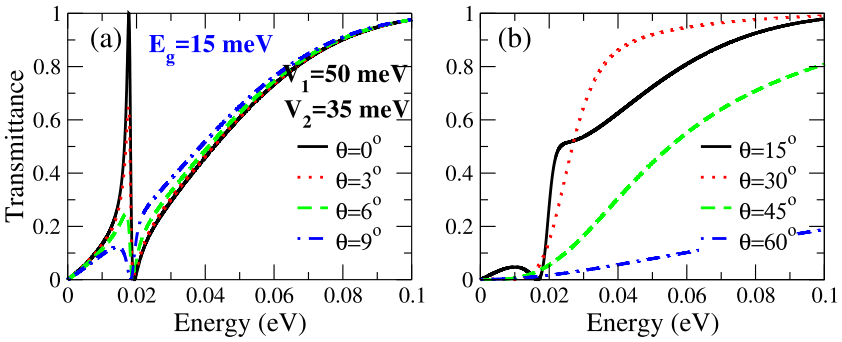

Fig. 6. Evolution of Fano resonances as a function of the angle of incidence for bilayer graphene single barriers under a bandgap opening of E_g = 15 meV. In (a) we are considering angles of incidence near to normal incidence, while in (b) the angles are far from normal incidence. Here, the barrier width is 10 nm, V_1 = 50 meV and V_2 = 35 meV, which results in the above mentioned bandgap, $E_g = V_1 - V_2 = 15$ meV.

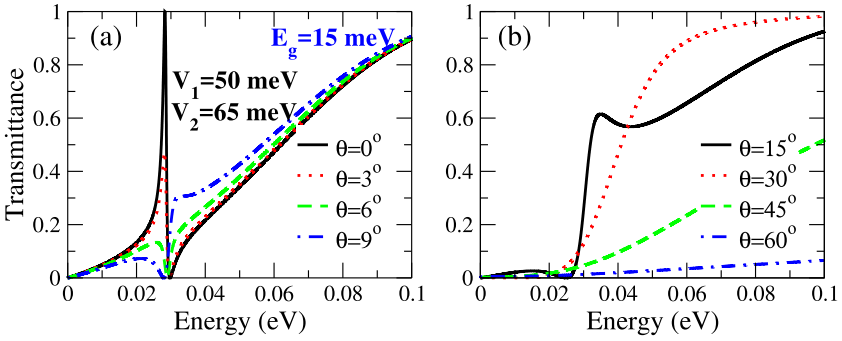

Fig. 7. The same as Fig. 6, however here V_1 = 65 meV and V_2 = 50 meV.

compare the solid-black curves in Fig. 8. However, once the bandgap is opened and it is modulated appropriately the conductance will manifest directly the asymmetrical line-shape typical of the Fano profile without the need of reducing the angular range, see the long-dashed-red and short-dashed-green curves in Fig. 8a and b. We obtain a similar trend if we keep fixed V_1 and varied V_2 than if we fixed V_2 and varied V_1. However, in the former case the conductance Fano-like profile is shifted to lower energies, while in the latter the profile is shifted to higher energies. In addition, in the former the Fano-like profile is better defined because the main contribution comes from the newly Fano resonances activated by the bandgap opening, see Fig. 6. In the case of the dotted–dashed-blue curves it is difficult to relate them to the Fano resonances because by reducing the angular range the resulting profiles are far from the typical asymmetrical line-shape of Fano resonances, see Fig. 8c and d. We consider that this results are quite relevant because they open the possibility of test the exotic phenomenon of Fano resonances in bilayer graphene structures without the need of angular discrimination. Although angular transport measurements in graphene are nowadays a reality [37,38], it is always welcomed (better) to have a direct measurement of the conductance without the possible intricacies associated to the angular resolution. It is also important to remark that the signatures of the Fano resonances are clearly identifiable in the transport properties with the conductance Fano-like profile and that the energy range at which it is taking place (10 meV) is totally reachable from the experimental standpoint. In fact, the conductance Fano-like profile is more evident than the hallmark in the conductance reported for cloaked states [19].

3.2. Double barrier structures

Regarding gapless bilayer graphene double barriers it is known that the coupling between Fano resonances and the natural resonances of the well region results in the so-called hybrid resonances [26], in analogy with the resonances that arise in the optical phenomena [39]. The main characteristic of these resonances is a total reflection region, pronounced dip, surrounded by transmission maxima. It is also important to mention that in the gapless case this resonance is only presented at oblique incidence and small angles of incidence. In Fig. 9a we can see how a well-defined hybrid resonance at $\theta = 5°$ is affected by the bandgap opening. In this case V_1 has been fixed to 50 meV and V_2 was varied from 50 meV to 20 meV in steps of 10 meV. The widths of the barriers and the well are the same and equal to 10 nm. As we can notice once the bandgap is opened (E_g = 10 meV) the left peak of the hybrid resonances is diminished and shifted to lower energies. By systematically increasing the bandgap the hybrid resonance continuously lose its hybrid profile, that is, the left peak shifts to lower energies and after diminishing starts to increase until it merges with another transmission maximum forming a double resonance. On the contrary, the right peak keeps its energy location and increases as the bandgap gets larger. So, at first instance the bandgap opening is not beneficial for hybrid resonance because it deforms and practically destroys the hybrid profile. However, as in the case of single barriers, the bandgap opening activates another transmission channels that sustain hybrid resonances. For instance, hybrid resonances are presented at normal incidence under bandgap opening. As we can see in Fig. 9b for the gapless case (solid-black curve) the invisibility of discrete states forbids the formation of the Fano resonances and consequently the emergence of hybrid resonances. So, what we see at normal incidence is essentially a resonance that come from the quantum well region, located at about 25 meV. Once the bandgap is opened the invisibility is broken and the effective coupling between Fano and quantum well resonances gives rise to the hybrid profile, see the long-dashed-red curve in Fig. 9b. By further increasing the bandgap the hybrid profile is deformed and practically lost, in similar fashion as the case of oblique incidence Fig. 9a. If now we keep fixed V_2 and varied V_1 from 50 meV to 80 meV in steps of 10 meV the results are not necessarily the same as in the preceding case. For instance, in the oblique case ($\theta = 5°$) when the bandgap is small the hybrid resonance is moved to higher energies and

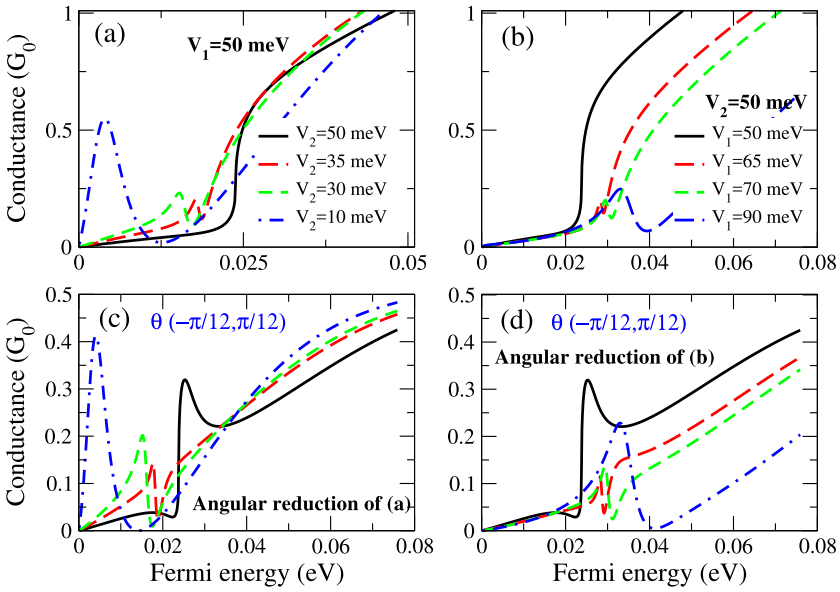

Fig. 8. Conductance versus the Fermi energy for different values of the bandgap. In (a) we have fixed V_1 and varied V_2, while in (b) V_2 is fixed and V_1 is varied. (c) and (d) are angular reductions of (a) and (b) respectively, that is, the integral for the conductance has been computed from $-\pi/12$ to $\pi/12$. As in the preceding figures the width of the barrier is 10 nm.

diminished, see the long-dashed-red curve in Fig. 10a. In addition, for a bandgap of 20 meV (V_1 = 70 meV) the resonances is so deformed that it is difficult to consider it as an hybrid resonance. In particular, we have a depressed maximum with minima and even smaller maxima at the sides. For a bandgap of 30 meV (V_1 = 80 meV) the transmittance profile is so deformed that is far from the typical profile for hybrid resonances. Essentially we have two peaks, one at 25 meV and the other at 40 meV. In the case of normal incidence we can see that the hybrid resonance is more pronounced and it is presented with a double resonance at the low-energy side, see long-dashed-red curve in Fig. 10b. Here, it is important to remark that the resonance at lowest energy has a Fano-like profile. So, when we increase the bandgap to 20 meV the double peaks become an hybrid resonance with highly reduced peaks. For a bandgap of 30 meV the transmittance has changed hugely such that it is not possible to consider it as the typical hybrid profile, see the dotted–dashed-blue curve in Fig. 10b. At the light of these results it seems better for the possible detection of hybrid resonances as well as the possible use of them in practical devices to keep fixed V_1 and varied V_2.

Now it is turn to analyze the impact of the angle of incidence over hybrid resonances in gapped double barriers. This parameter is quite relevant because it is directly related to the transport properties. In Fig. 11 we show the evolution of hybrid resonances with the angle of incidence. We have considered gapped double barriers with V_1 = 50 meV and V_2 = 40 meV and V_1 = 60 meV and V_2 = 50 meV, Fig. 11a and b, respectively. The widths of the barriers and the well are the same as in the preceding figures, namely: $dB_1 = dB_2 = dW$ = 10 nm. In Fig. 11a we see a well-defined hybrid resonance at normal incidence (solid-black curve) that when the angle of incidence is increased it is systematically diminished, especially the peak at low energy, compare the solid-black and long-dashed-red curves. As in the case of Fano resonances in single barriers after 15° the hybrid profile is totally lost, see the dotted–dashed-blue curve in Fig. 11a. One aspect that is important to highlight here it is that despite the deformation and destruction of the hybrid profile with the angle of incidence there are no other contributions in the energy window at which the hybrid resonance is presented. So, we can expect that the hybrid profile be also manifested in the conductance curves. As similar evolution for the hybrid resonances is obtained in Fig. 11b. However in this case the peaks of the hybrid resonances are not as prominent as in Fig. 11a. So, it is expected that the signatures of hybrid resonances on the conductance not be as evident and prominent as in the case of Fig. 11a.

Regarding the transport properties, in Fig. 12 we show the conductance as a function of the Fermi energy for different values of the bandgap. In Fig. 12a we have fixed V_1 at 50 meV and varied V_2 from 50 meV to 20 meV in steps of 10 meV, while in Fig. 12b V_2 is fixed and V_1 is varied from 50 meV to 80 meV in steps of 10 meV. As we can see in Fig. 12a a hybrid profile arise in the conductance for gapless barriers (solid-black curve) at about 27 meV. One of the main characteristics of this profile is its acuteness, with a peak at the left side and a pronounced rise at the right side. The effective with of the hybrid resonance is less than 5 meV, which could be a difficulty from the experimental standpoint. By opening the bandgap the conductance hybrid profile is shifted to lower energies and the effective width of it increases as well, see the long-dashed-red curve in Fig. 12a. This effective broadening of the profile is welcomed because it could help to resolve and detect easily the contribution of hybrid resonance in electron transport measurements. We can also see two other main contribution to the conductance, an acute peak at intermediate energy (15 meV) and a broad peak at low energy (10 meV). The intermediate acute peak come from the intricate deformation of the hybrid resonance as the angle of incidence is increased, while the broad peak at low energy is related to Breit–Wigner resonances, which are dominant in that energy region as the angle of incidence increases. For larger bandgaps the conductance hybrid profile is systematically deformed and eventually lost, see for instance the dotted–dashed-blue curve in Fig. 12a. In the case of V_1 = 60 meV and V_2 = 50 meV (Fig. 12b) we obtain similar results. However, in this case the hybrid profile is shifted to higher energies and the peaks are not as prominent as in Fig. 12a. So, in trying to detect the contribution of hybrid resonances on the transport properties is quite relevant to tune appropriately the bandgap.

Now we study the intrinsic structural asymmetry of double barrier structures. In particular, we analyze the impact on the transmission and transport properties of the asymmetry associated to the width of the barriers, the thickness of the well and the bandgap in the barrier regions. In Fig. 13 we show the results of the asymmetry related to the well width. We have systematically reduced the well width from 10 nm to 2.5 nm in steps of 2.5 nm. The other double barrier parameters are fixed to dB_1 = dB_2 = 10 nm, V_1 = 50 meV and V_2 = 40 meV.

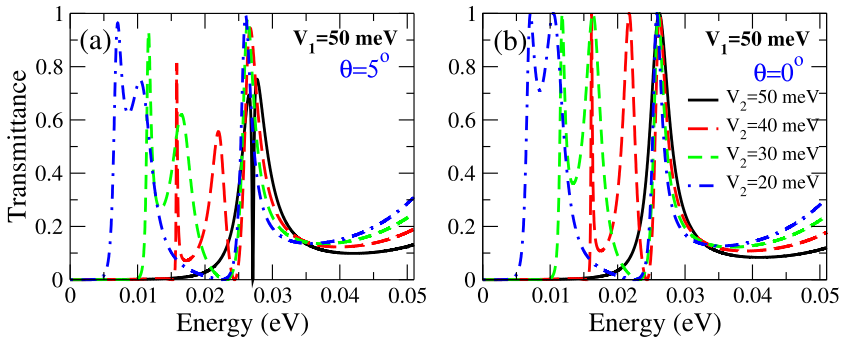

Fig. 9. Bandgap effect over hybrid resonances in double barrier structures. (a) Evolution of a well-defined hybrid resonance at oblique incidence ($\theta = 5°$) for different values of the bandgap. (b) The same as (a) but for normal incidence ($\theta = 0°$). Here, V_1 is fixed and V_2 is varied. The widths of the barriers and the well is the same $dB_1 = dB_2 = dW = 10$ nm.

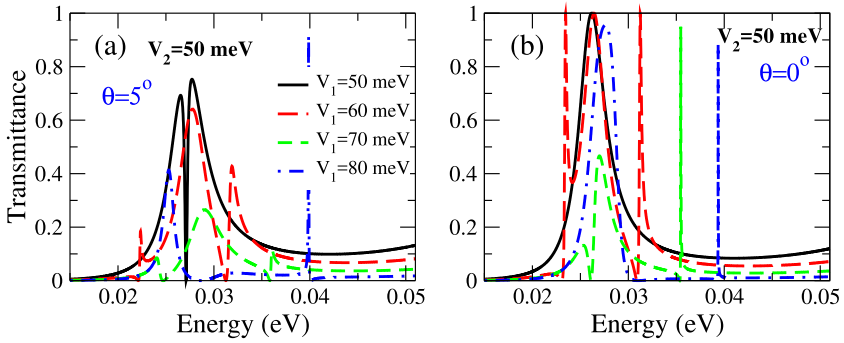

Fig. 10. The same as Fig. 9, but here V_2 is fixed and V_1 is varied as shown.

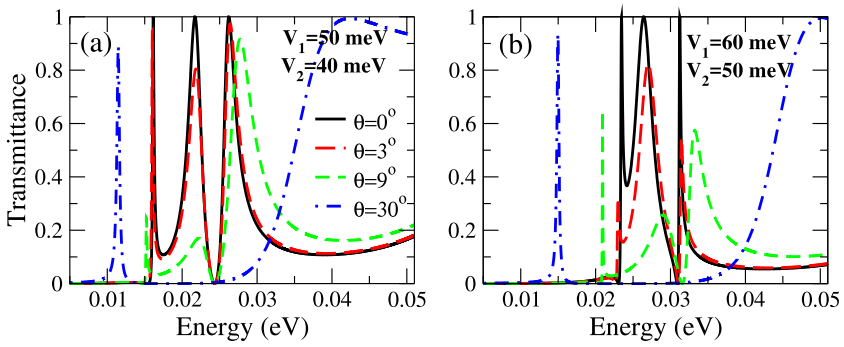

Fig. 11. Influence of the angle of incidence over hybrid resonances in gapped double barrier structures. The bandgap considered is $E_g = 10$ meV. In (a) V_2 is diminished 10 meV respect to the reference (gapless) case (50 meV), while in (b) V_1 is increased 10 meV with respect to the reference case.

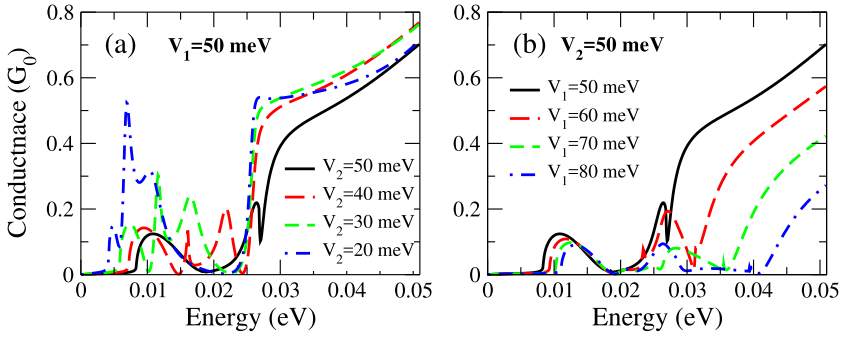

Fig. 12. Conductance versus the Fermi energy in double barrier structures for different values of the bandgap. In (a) we have fixed V_1 and varied V_2, while in (b) V_2 is fixed and V_1 is varied. The solid-black, long-dashed-red, short-dashed-green and dotted–dashed curves correspond to the gapless case, a bandgap of 10, 20 and 30 meV, respectively. The widths of the barriers and well are the same $dB_1 = dB_2 = dW = 10$ nm.

The solid-black and dashed-red curves correspond to normal incidence ($\theta = 0°$) and oblique incidence ($\theta = 5°$), respectively. In the symmetric case (Fig. 13a) we can see a well-defined hybrid resonance at normal incidence promoted by the bandgap opening $E_g = V_1 - V_2 = 10$ meV. At oblique incidence, the low-energy peak of the hybrid resonance is diminished. We can also see an acute peak at low energy for both normal and oblique incidence. Once the asymmetry of the well width is incorporated, the hybrid resonance is distorted. In particular, for normal incidence the low- and high-energy peaks of the hybrid resonance separate systematically each other as the well width decreases, being the low-energy peak narrower and the high-energy peak broader, see the solid-black curves in Fig. 13b, c and d. We also notice an effective shift of the peaks of the hybrid resonance to high energies as well as a shift to low energies of the acute peak originally located at about 0.015 eV. At oblique incidence we see a similar dynamic for the hybrid resonance. However, the low-energy peak is systematically reduced as the well width increases. Likewise, the acute peak close to 0.015 eV diminishes and practically disappears after $dW = 5.0$ nm. This asymmetry allows us to see that the hybrid resonance is the result of the interplay between a resonance of the barriers and a resonance of the well. In specific, the resonance of the well region moves to higher energies as the well width grows, deteriorating the coupling that gives rise to the hybrid resonance. In the limit of zero well width we will have the transmission properties of a single barrier of a width of 20 nm. Quite different results are obtained when we increase the well width rather than reduce it, see Fig. 14. By increasing the well width the resonances associated to the well region move to lower energies, resulting in a more intricate coupling with the resonances of the barriers. For instance, for $dW = 12.5$ nm, at normal incidence, the hybrid resonance has transformed in two Fano resonances with one broad resonance in between them. For $dW = 15.0$ nm, the Fano resonance in the low-energy side disappeared and the one in the high-energy side is reverted. In the case of $dW = 17.5$ nm, the broad resonance shifts to the low-energy side and two Fano resonances appear at high energies. Similar results are obtained for oblique incidence, however the peaks related to the Fano resonances are not as prominent as in the case of normal incidence, compare the solid-black and dashed-red curves in Fig. 14b, c and d.

Regarding the transport properties, Fig. 15 shows the impact of the asymmetry of the well width on the conductance. Fig. 15a corresponds to the double barriers of Fig. 13, while Fig. 15b to the double barriers of Fig. 14. As we can notice, once the asymmetry of the well width is incorporated, the characteristics of the hybrid resonances are no longer visible in the conductance. In particular, when the well width is decreased (Fig. 15a) the conductance presents two peaks, being the low-energy peak dominant. The energy location of these peaks coincides with the energy of the resonances associated to the barriers, see Fig. 13. On the contrary, when the well width is increased (Fig. 15b) the conductance presents multiple peaks due to the intricate interplay between the resonances of the barriers and the well.

Now it is turn to analyze the impact of having barriers of different width. In this case, we have fixed dB_1 to 10 nm and varied dB_2. The well width and the potentials are also fixed to $dW = 10$ nm, $V_1 = 50$ meV and $V_2 = 40$ meV. In Figs. 16 and 17 we show the results for the transmission when dB_2 is reduced and increased, respectively. In both figures, the solid-black and dashed-red curves correspond to transmission at normal ($\theta = 0°$) and oblique incidence ($\theta = 5°$), respectively. As we can notice in Fig. 16, when the second barrier is reduced the hybrid resonance profile is not lost at all as in the case of reducing the well width (Fig. 13). For instance, at normal incidence, the well-defined hybrid resonance profile of the symmetric case (Fig. 16a) is systematically transformed as dB_2 decreases till it emerges as a Fano profile for $dB_2 = 2.5$ nm. In particular, we can see that the high-energy peak of the hybrid resonance diminishes as dB_2 is reduced. For oblique incidence we have a similar dynamic, however, the hybrid resonance transforms systematically till it adopts an anti-resonance profile for $dB_2 = 2.5$ nm. In the limit of zero dB_2 we will have the transmission properties of a single barrier with a thickness of 10 nm. When we increase dB_2, the interplay between the resonances of the barriers and the well is more intricate. In fact, the low-energy peak of the hybrid resonance is practically unaffected when dB_2 grows. On the contrary, the high-energy peak of the hybrid resonance and the narrow resonance in the low-energy side are greatly affected, becoming Fano-like resonances for large dB_2. This happens for normal and oblique incidence, however, for the latter, the peaks are not as prominent as for the former. All these transmission characteristics will be reflected in great extent in the transport properties.

In Fig. 18 we present the transport properties of the symmetry associated to dB_2. When we reduce dB_2 (Fig. 18a) the typical conductance curve of the symmetric case (solid-black curve) is systematically modified till it looks like the conductance curve of a single barrier. The first effect of this type of asymmetry is the disappearance of the acute conductance peak located at about 0.015 eV, compare solid-black and dashed-red curves in Fig. 18a. Secondly, the broad peaks at 0.01 eV and 0.02 eV shift to lower energy and get narrow, being the former predominant (higher) than the latter. Furthermore, as dB_2 approaches to zero the high and acute peak in the low-energy side will disappear and the conductance curve will be of a single barrier, see Fig. 8a. On the other hand, the conductance curves are quite different when we increase dB_2. For instance, the conductance curve of the symmetric case is barely affected with a small increase in dB_2, see the long-dashed-red curve in Fig. 18b. In fact, the whole curve is shifted to higher energies, but the envelope is preserved. For $dB_2 = 15$ nm we see an additional shift of the curve to higher energies as well as a broad peak in the high-energy side. For $dB_2 = 17.5$ nm, two extra peaks are presented in the conductance, in addition to the systematic shift of the curve, a small one about 0.03 eV and a huge one close to zero, see the dotted–dashed-blue curve in Fig. 18b.

The last asymmetry we will address is the one that is presented when the barriers have different bandgaps. In Fig. 19 we show the impact of this type of asymmetry on the transmission properties. In this case, we have fixed the bandgap of the first barrier, $E_g^{B_1} = 10$ meV, and varied the bandgap of the second one, $E_g^{B_2}$. The width of the barriers and well is the same $dB_1 = dB_2 = dW = 10$ nm. As in the preceding asymmetries, we have considered normal and oblique incidence, solid-black and dashed-red curves, respectively. As we can see this asymmetry is quite peculiar. The main effect of it is to reduce or increase the distance between the peaks of the hybrid resonance. For instance, when $E_g^{B_2} = 0$ meV the distance between the peaks is diminished, resulting in a narrower hybrid profile, see Fig. 19b. On the contrary, when $E_g^{B_2}$ gets larger the peaks separate each other, resulting in a broader hybrid resonance, see Fig. 19c and d. This happens for both normal and oblique incidence, with small differences in the intensities of the peaks. These characteristics are also manifested in the transport properties (Fig. 20). In fact, the conductance presents a narrow or broad hybrid-like profile depending if $E_g^{B_2}$ is reduced or increased.

As we have corroborated, the intrinsic asymmetries of double barrier structures can be used as tuning parameters to modulate the transmission and transport properties. In addition, the asymmetries can helps us to unveil the origin of the different resonances and peaks presented in the transmission and conductance curves.

4. Conclusions

In summary, we address the exotic phenomenon of Fano resonances in bilayer graphene single and double barrier structures. In particular, we study how these resonances are modified by bandgap opening in the band structure of bilayer graphene. A four-band hamiltonian has been used to describe electrons as well as to incorporate the mentioned band structure modifications. The hybrid matrix method and the Landauer–Büttiker formalism were implemented to obtain the transmittance and the conductance, respectively. We find that bandgap opening promotes

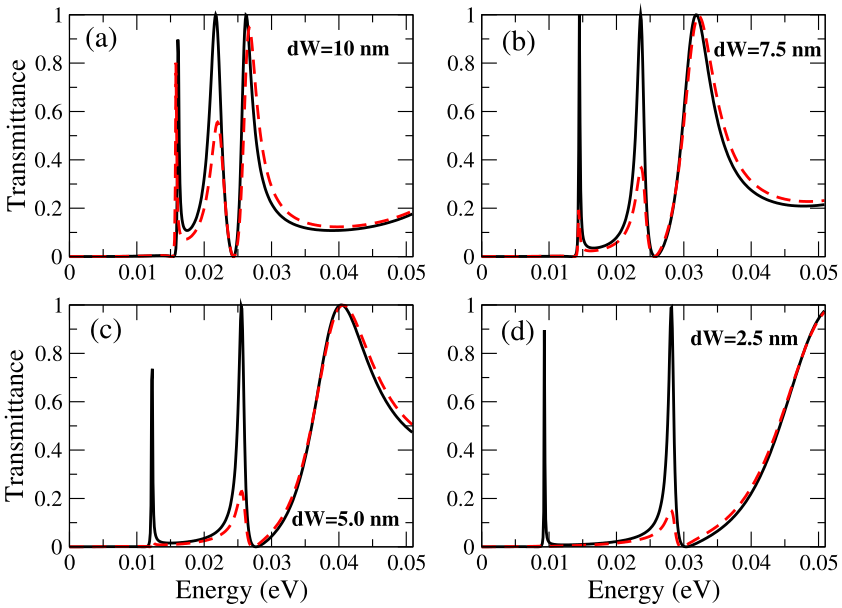

Fig. 13. Impact of the asymmetry of the well width on the transmission of double barrier structures. The well widths considered are (a) 10 nm, (b) 7.5 nm, (c) 5.0 nm and (d) 2.5 nm. The other double barrier parameters are fixed to $dB_1 = dB_2 = 10$ nm, $V_1 = 50$ meV and $V_2 = 40$ meV. The solid-black curves correspond to normal incidence $\theta = 0°$, while the dashed-red ones to $\theta = 5°$.

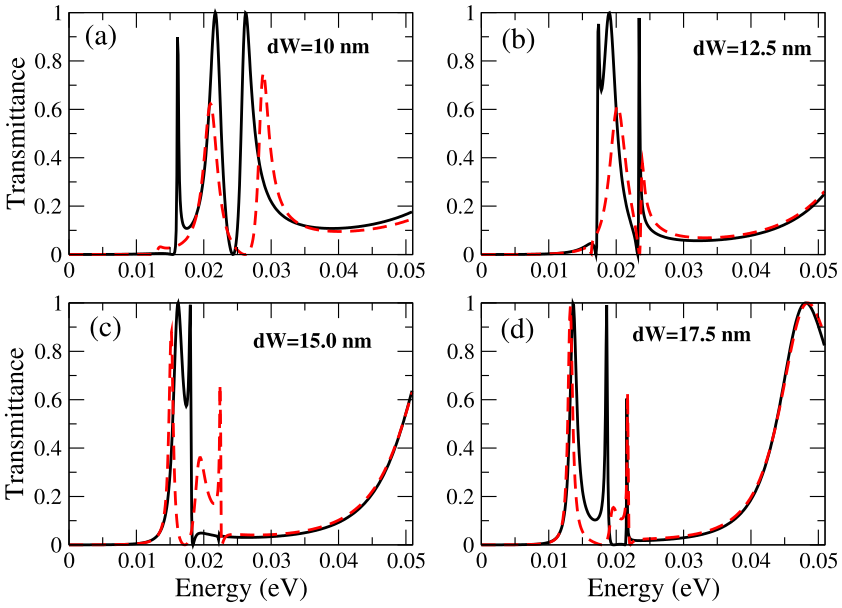

Fig. 14. The same as Fig. 13, but here the well widths are (a) 10 nm, (b) 12.5 nm, (c) 15.0 nm and (d) 17.5 nm.

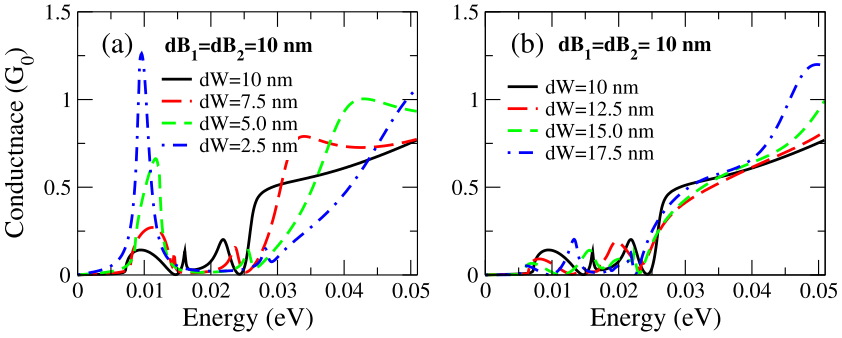

Fig. 15. Impact of the asymmetry of the well width on the conductance of double barrier structures. (a) The well width is systematically reduced from 10 nm to 2.5 nm in steps of 2.5 nm. (b) The well width is systematically increased from 10 nm to 17.5 nm in steps of 2.5 nm. The widths and heights of the barriers are the same as in Figs. 13 and 14.

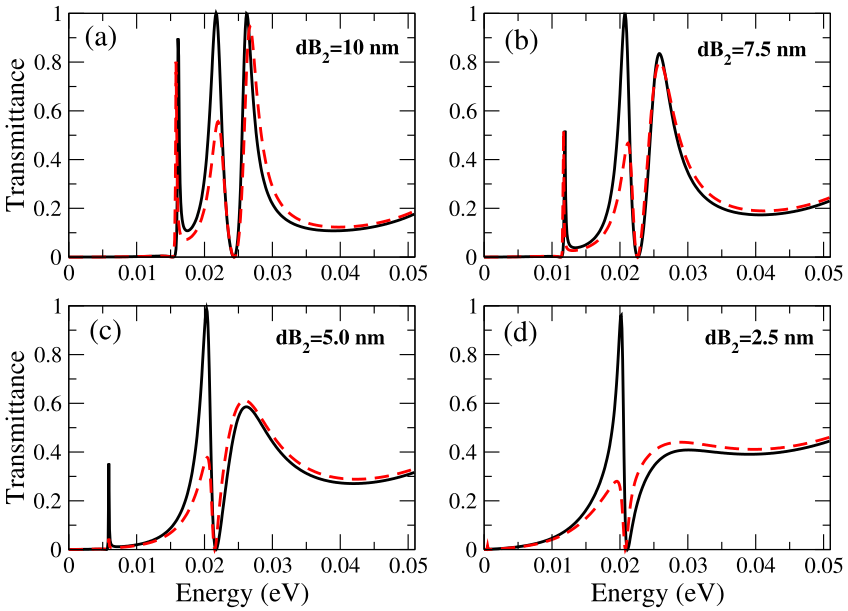

Fig. 16. Impact of the asymmetry associated to the width of the barriers on the transmission of double barrier structures. The widths considered for the second barrier are (a) 10 nm, (b) 7.5 nm, (c) 5.0 nm and (d) 2.5 nm. The other double barrier parameters are fixed to $dB_1 = dW = 10$ nm, $V_1 = 50$ meV and $V_2 = 40$ meV. The solid-black curves correspond to normal incidence $\theta = 0°$, while the dashed-red ones to $\theta = 5°$.

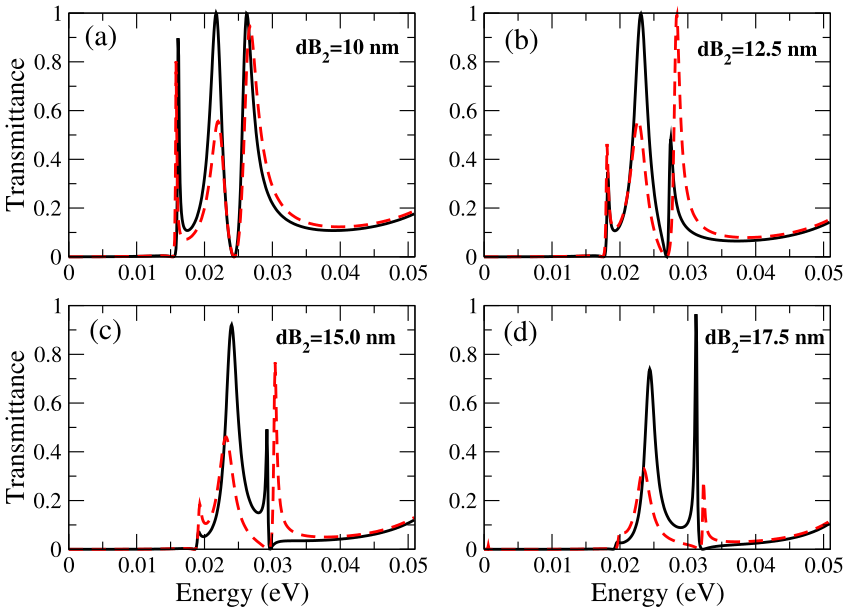

Fig. 17. The same as Fig. 16, but here the widths of the second barrier are (a) 10 nm, (b) 12.5 nm, (c) 15.0 nm and (d) 17.5 nm.

the coupling between extended and discrete states, resulting in Fano resonances at transmission channels that were not activated in the gapless case. For instance, we find that with a small bandgap the Fano line-shape is presented in the transmittance at normal incidence for single barrier structures. In the case of double barriers we also find hybrid Fano resonances at normal incidence. The improvement of the chiral matching between extended and discrete states induced by the bandgap opening results in an effective enhancement of the Fano response on the transport properties. In particular, we can identify the Fano contribution in the conductance without the need of reducing the angular range. In the case of single barriers a Fano line-shape is presented in the conductance, while for double barriers a hybrid profile can be identified in the conductance straightforwardly. So, bandgap opening far from disrupts and destroys the Fano response promotes it and can be used as a tuning parameter to corroborate the exotic phenomenon of Fano resonances in bilayer graphene barrier structures.

Declaration of competing interest

The authors declare that they have no known competing financial interests or personal relationships that could have appeared to influence the work reported in this paper.

CRediT authorship contribution statement

J.A. Briones-Torres: Methodology, Software, Data curation, Investigation, Writing - reviewing & editing. **R. Pérez-Álvarez:** Writing - reviewing & editing. **R. Pernas-Salomón:** Methodology, Writing -

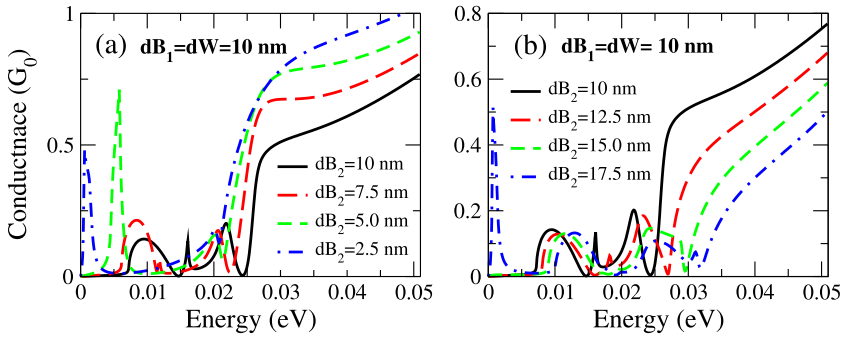

Fig. 18. Impact of the asymmetry related to the width of the barriers on the conductance of double barrier structures. (a) The width of the second barrier is systematically reduced from 10 nm to 2.5 nm in steps of 2.5 nm. (b) The width of the second barrier is systematically increased from 10 nm to 17.5 nm in steps of 2.5 nm. The other double barrier parameters are the same as in Figs. 16 and 17.

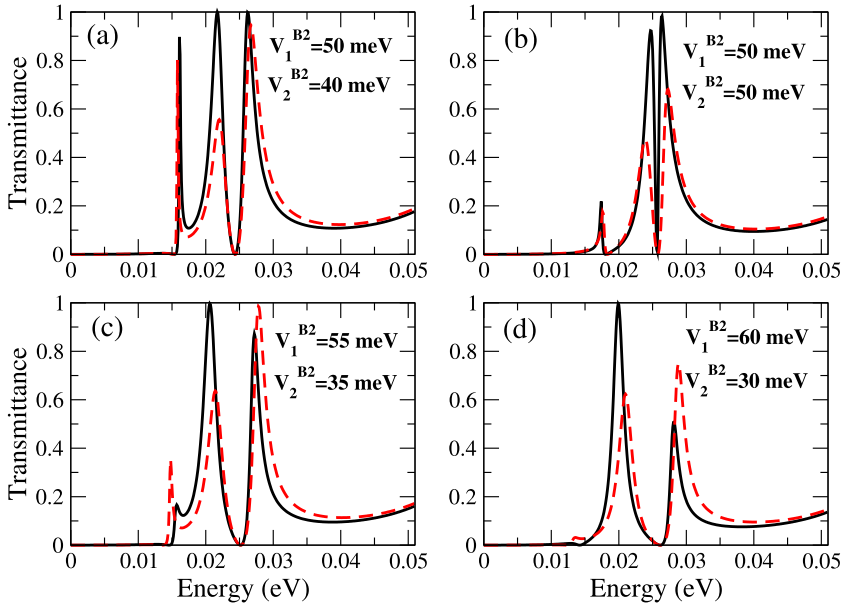

Fig. 19. Impact of the asymmetry associated to barriers with different bandgap on the transmission of double barrier structures. The bandgap of the first barrier $E_g^{B_1} = V_1^{B_1} - V_2^{B_1}$ is fixed to 10 meV, while the one of the second barrier $E_g^{B_2} = V_1^{B_2} - V_2^{B_2}$ is varied: (a) 10 meV, (b) 0 meV, (c) 20 meV and (d) 30 meV. The widths of the barriers and well are the same $dB_1 = dB_2 = dW = 10$ nm and remain fixed. The solid-black and dashed-red curves correspond to normal ($\theta = 0°$) and oblique ($\theta = 5°$) incidence, respectively.

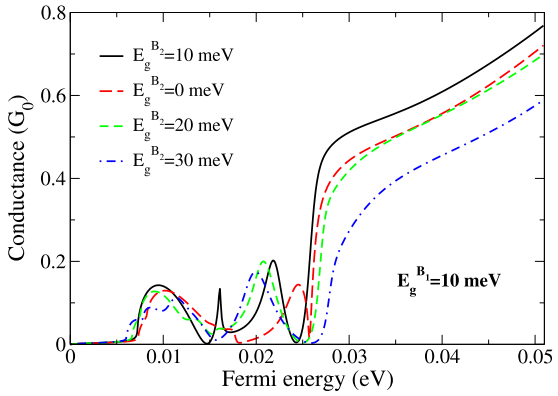

Fig. 20. The same as in Fig. 19, but for the conductance.

reviewing & editing. **I. Rodríguez-Vargas:** Conceptualization, Investigation, Writing - original draft, Visualization, Funding acquisition.

Acknowledgments

J.A.B.-T. acknowledges to PRODEP-SEP-Mexico for the Postdoctoral Research Fellowship 511-6/2019-10959. R.P.Á. acknowledges to Autonomous University of Zacatecas for the hospitality. I.R.-V. would like to acknowledge to CONACYT-SEP Mexico for the financial support through grant A1-S-11655.

Appendix A. Supplementary data

Supplementary material related to this article can be found online at https://doi.org/10.1016/j.physe.2020.113999.

References

[1] M.I. Katsnelson, Carbon in two dimensions, Mater. Today 10 (2007) 20.
[2] A.K. Geim, K.S. Novoselov, The rise of graphene, Nature Mater. 6 (2007) 183.
[3] E. McCann, M. Koshino, The electronic properties of bilayer graphene, Rep. Progr. Phys. 76 (2013) 056503.
[4] C.R. Dean et. al, Boron nitrite substrates for high-quality graphene electronics, Nature Nanotechnol. 5 (2010) 722.

[5] A.A. Balandin, Thermal properties of graphene and nanostructured carbon materials, Nature Mater. 10 (2011) 569.
[6] K.S. Novoselov et. al, Unconventional quantum Hall effect and Berry's phase of 2π in bilayer graphene, Nature 2 (2006) 177–180.
[7] K.S. Novoselov, et al., Electric field effect in atomically thin carbon films, Science 306 (2004) 666.
[8] Y. Zhang et. al, Direct observation of a widely tunable bandgap in bilayer graphene, Nature 459 (2009) 820–823.
[9] E.V. Castro et. al, Biased bilayer graphene: semiconductor with a gap tunable by the electronic field effect, Phys. Rev. Lett. 99 (2007) 216802.
[10] A.H. Castro Neto, F. Guinea, N.M.R. Peres, K.S. Novoselov, A.K. Geim, The electronic properties of graphene, Rev. Modern Phys. 81 (2009) 109.
[11] M.I. Katsnelson, K.S. Novoselov, A.K. Geim, Chiral tunneling and the Klein paradox in graphene, Nat. Phys. 2 (2006) 620.
[12] A.F. Young, P. Kim, Quantum interference and Klein tunnelling in graphene heterojunctions, Nature Phys. 5 (2009) 222–226.
[13] A.V. Shytov, M.I. Katsnelson, L.S. Levitov, Atomic collapse and Quasi–Rydberg states in graphene, Phys. Rev. Lett. 99 (2007) 246802.
[14] Y. Wang, et al., Observing atomic collapse resonances in artificial nuclei on graphene, Science 340 (2013) 734–737.
[15] L.A. Ponomarenko, et al., Cloning of dirac fermions in graphene superlattices, Nature 497 (2013) 594–597.
[16] C.R. Dean, et al., Hofstadter's butterfly and the fractal quantum hall effect in moire superlattices, Nature 497 (2013) 598–602.
[17] V.V. Cheianov, V. Fal'ko, B.L. Altshuler, The focusing of electron flow and a Veselago lens in graphene p–n junctions, Science 315 (2007) 1252–1255.
[18] S. Chen, et al., Electron optics with p–n junctions in ballistic graphene, Science 353 (2016) 1522–1525.
[19] N. Gu, M. Rudner, L. Levitov, Chirality-assisted electronic cloaking of confined states in bilayer graphene, Phys. Rev. Lett. 107 (2011) 156603.
[20] K. Lee, S. Lee, Y.S. Eo, C. Kurdak, Z. Zhong, Evidence of electronic cloaking from chiral electron transport in bilayer graphene nanostructures, Phys. Rev. B 94 (2016) 205418.
[21] R. Bistritzer, A.H. MacDonald, Moiré bands in twisted double-layer graphene, Proc. Natl. Acad. Sci. USA 108 (2011) 12233.
[22] Y. Cao, et al., Unconventional superconductivity in magic-angle graphene superlattices, Nature 556 (2018) 43.
[23] S. Mukhopadhyay, R. Biswas, C. Sinha, Signature of quantum interference and the Fano resonances in the transmission spectrum of bilayer graphene nanostructure, J. Appl. Phys. 110 (2011) 014306.
[24] S. Mukhopadhyay, R. Biswas, C. Sinha, Tunable Fano resonances in the ballistic transmission and tunnelling lifetime in a biased bilayer graphene nanostructure, Phys. Lett. A 375 (2011) 2921–2927.
[25] C. Sinha, R. Biswas, Unconventional ballistic transport through bilayer graphene electrostatic barriers, Phys. Rev. B 84 (2011) 155439.
[26] J.A. Briones-Torres, I. Rodríguez-Vargas, Fano resonances in bilayer graphene superlattices, Sci. Rep. 7 (2017) 16708.
[27] A.E. Miroshnichenko, S. Flach, Y.S. Kivshar, Fano resonances in nanoscale structures, Rev. Modern Phys. 82 (2010) 2257.
[28] T.T. Tang, et al., A tunable phonon–exciton Fano system in bilayer graphene, Nature Nanotechnol. 5 (2010) 32–36.
[29] A.B. Kuzmenko, et al., Gate tunable infrared phonon anomalies in bilayer graphene, Phys. Rev. Lett. 103 (2009) 116804.
[30] W. Lu, W. Li, C. Xu, C. Ye, Destruction of anti-Klein tunneling induced by resonant states in bilayer graphene, J. Phys. D: Appl. Phys. 48 (2015) 285102.
[31] J.A. Briones-Torres, R. Pernas-Salomón, R. Pérez-Álvarez, I. Rodríguez-Vargas, Hybrid matrix method for stable numerical analysis of the propagation of Dirac electrons in gapless bilayer graphene, Superlattices Microstruct. 93 (2016) 186–201.
[32] E.L. Tan, Hybrid compliance-stiffness matrix method for stable analysis of elastic wave propagation in multilayered anisotropic media, J. Acoust. Soc. Am. 119 (2006) 45–53.
[33] R. Pérez-Álvarez, R. Pernas-Salomón, V.R. Velasco, Relations between transfer matrices and numerical stability analysis to avoid the Ωd problem, SIAM J. Appl. Math. 75 (2015) 1403–1423.
[34] M. Barbier, P. Vasilopoulos, F.M. Peeters, J. Milton Pereira, Jr, Bilayer graphene with single and multiple electrostatic barriers: Band structure and transmission, Phys. Rev. B 79 (2009) 155402.
[35] S. Datta, Electronic Transport in Mesoscopic Systems, Cambridge University Press, 1995.
[36] A. Varlet, M.-H. Liu, D. Bischoff, P. Simonet, T. Taniguchi, K. Watanabe, K. Richter, T. Ihn, K. Ensslin, Band gap and broken chirality in single-layer and bilayer graphene, Phys. Status Solidi 10 (2016) 46–57.
[37] S. Sutar, E.S. Comfort, J. Liu, T. Taniguchi, K. Watanabe, J.U. Lee, Angle-dependent carrier transmission in graphene p–n junctions, Nano Lett. 12 (2012) 4460–4464.
[38] A. Rahman, J.W. Guikema, N.M. Hassan, N. Markovic, Angle-dependent transmission in graphene heterojunctions, Appl. Phys. Lett. 106 (2015) 013112.
[39] K.A. Yasir, W.-M. Liu, Controlled electromagnetically induced transparency and Fano resonances in hybrid BEC-optomechanics, Sci. Rep. 6 (2016) 22651.